ACS APPLIED MATERIALS & INTERFACES

www.acsami.org

Research Article

# Order−Disorder Phase Transition and Ionic Conductivity in a $Li_2B_{12}H_{12}$ Solid Electrolyte

Alexey P. Maltsev,* Ilya V. Chepkasov, and Artem R. Oganov

Cite This: *ACS Appl. Mater. Interfaces* 2023, 15, 42511−42519

Read Online

ACCESS | Metrics & More | Article Recommendations | Supporting Information

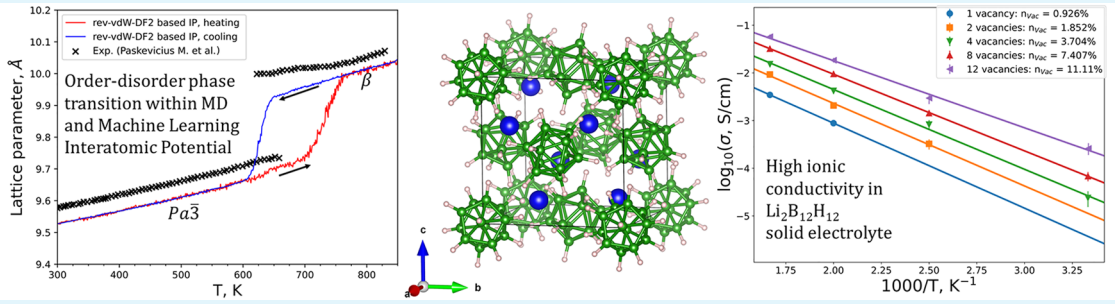


**ABSTRACT:** Temperature-induced phase transitions and ionic conductivities of $Li_2B_{12}H_{12}$ and $LiCB_{11}H_{12}$ were simulated with the use of machine learning interatomic potentials based on van der Waals-corrected density functional theory (rev-vdW-DF2 functional). The simulated temperature of order−disorder phase transition, lattice parameters, diffusion, ionic conductivity, and activation energies are in good agreement with experimental data. Our simulations of $Li_2B_{12}H_{12}$ uncover the importance of the reorientational motion of the $[B_{12}H_{12}]^{2-}$ anion. In the ordered $\alpha$-phase ($T$ < 625 K), these anions have well-defined orientations, while in the disordered $\beta$-phase ($T$ > 625 K), their orientations are random. In vacancy-rich systems, its complete rotation was observed, while in the ideal crystal, the anions display limited vabrational motion, indicating the static nature of the phase transition without dynamic disordering. The use of machine learning interatomic potentials has allowed us to study large systems (>2000 atoms) in long (nanosecond-scale) molecular dynamics runs with ab initio quality.

**KEYWORDS:** *density functional theory, machine learning interatomic potential, solid electrolyte, phase transition, ionic conductivity*



## 1. INTRODUCTION

Widely studied since the 1970s, Li-ion batteries have been in extensive use since the 1990s. However, despite numerous applications, they currently fail to meet the growing demand for higher energy storage densities, faster charging speeds, and lower costs. At the same time, further improvement of their design and operation has been limited.[1,2]

Switching to lithium metal instead of graphite as an anode is one possible avenue for the development of lithium-ion batteries. Metallic lithium has the highest theoretical gravimetric energy density (3860 mAh $g^{-1}$) and the lowest electrochemical potential (−3.04 V vs the standard hydrogen electrode) and is, therefore, traditionally considered to be the best material for the anode.[3,4] However, there are a number of factors that significantly limit its use and hinder its commercialization potential. These include safety issues and limited cyclability due to dendrite formation during the charge/discharge and low Coulomb efficiency.[4] Low Coulomb efficiency as well as the gradual increase in overvoltage of the lithium anode leads to a declining capacity during the cycling, whereas the growth of dendrites results in short circuits and thermal instability and often renders such batteries explosive. The primary way to solve these problems is the transition from liquid organic electrolytes to an inorganic solid electrolyte and all-solid-state batteries.[3,4] Solid electrolyte batteries offer greater safety and durability by preventing dendrite formation and short circuits. Their thermal stability and resistance to dendrite formation improve their cyclability, making them a reliable long-term option. Research shows that solid electrolyte batteries can maintain a current capacity of over 10,000 cycles.[5]

Over the past two decades, researchers have examined and synthesized solid electrolytes of various compositions, focusing on their characteristics such as transport, stability, and interfacial properties. The most commonly used compounds include Li−P−S−X (X = O, F, Cl, Br, I) and ceramics such as LATP, LLZO, LAGP, etc.[5−20] Despite these being among the most studied and showing good properties, there is an ongoing

Received: May 20, 2023
Accepted: August 1, 2023
Published: September 1, 2023

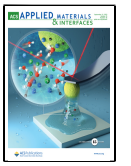




https://doi.org/10.1021/acsami.3c07242
*ACS Appl. Mater. Interfaces* 2023, 15, 42511−42519

interest in discovering new solid electrolytes. Metal dodecaboranes $M_{2/n}B_{12}H_{12}$ ($n$—valence of the metal M), for one, are notable for rechargeable metal batteries due to their high stability (our calculations show the enthalpy of the reaction of $Li_2B_{12}H_{12}$ with lithium being significantly higher than that in Li−P−S−X solid electrolytes) and ionic conductivity (~$10^{-4}$ S/cm at room temperature).

Recent years have seen a mounting body of both experimental and theoretical research focusing on the thermodynamic, transport, and interfacial properties of $Li_2B_{12}H_{12}$ and its related compounds.[21−32] Udovic et al. showed that $Na_2B_{10}H_{10}$ and $Na_2B_{12}H_{12}$ compounds are superionic with an ionic conductivity of about 0.1 S/cm at 400−500 K; such ionic conductivity is associated with the reorientation motion of $B_{12}H_{12}^{2-}$ ions.[26,27] In 2015, diffraction, spectroscopy, and theoretical simulations were used to corroborate that high conductivity is closely related to the phase transition from the ordered to disordered structure.[28] Lithium analogs of these compounds demonstrate similar results, so in $Li_2B_{12}H_{12}$, $LiCB_{11}H_{12}$, and $LiCB_9H_{10}$ compounds, the ionic conductivity reaches $10^{-2}$−$10^{-1}$ S/cm, as well as in mixed Li−Na compounds.[21,26,29,30] Although superionic behavior with conductivity $\sigma \sim 10^{-2}$−$10^{-1}$ S/cm is achieved only in high-temperature phases,[26,29−32] Tang et al. showed the possibility to obtain a high-temperature phase after cooling to 300 K without a back transition to the low-temperature phase.[32] At the same time, despite some materials having high transition temperatures, they can still be utilized as a solid electrolyte, like two commercial solid-state Na batteries (Na-S and ZEBRA), which operate near the temperature range of 550−620 K.[33,34]

Experimental studies of the ionic conductivity were backed by quantum chemical calculations using ab initio and classical molecular dynamics. Ab initio molecular dynamics (AIMD) simulations performed in ref 35 showed that modifying the anions and introducing cation defects improve diffusion properties. Classical molecular dynamics (MD) also supported this and revealed that asymmetric anions like $CB_{11}H_{12}$ enhance vacancy formation and increase ionic conductivity.[22,36] However, AIMD calculations are constrained by the short timescale and small system sizes, which often limits realism in the description of phase transitions. Also, such AIMD or other DFT calculations were performed using the PBE functional without any van der Waals corrections,[35,37,38] even though it was proven that van der Waals interactions cannot be neglected in these systems.[39] Moreover, in $Li_2B_{12}H_{12}$, within the PBE functional, the lowest energy phase differs from the experiment.[38] On the other hand, the use of MD with empirical potentials is usually much less reliable than DFT, making such simulations cheap but unrealistic. The use of machine learning interatomic potentials (MLIPs) for MD combines the advantages of both methods, namely, high accuracy and high efficiency. MLIPs and the use of active learning[40] have been successfully applied to many problems, including crystal structure prediction, studies of phase transitions and phase diagrams, calculations of thermodynamics, kinetic properties, etc.[41−47]

$Li_2B_{12}H_{12}$ is a promising material for solid electrolyte applications that combines high stability and ionic conductivity and has already been tested.[24] However, previous calculations do not fully match the experimental results, i.e., activation barriers of the low-temperature phase obtained by Varley et al.[35] are three times higher than the experimental values,[23] and MD simulations performed by Sau et al.[36] show no diffusion in the $\alpha$-phase. In this sense, there are still many gaps regarding theoretical calculations. In this work, we explore phase transitions, ionic conductivity, and $B_{12}H_{12}^{2-}$ anion behavior to obtain insights into kinetic properties with the use of accurate molecular dynamics and MLIPs fitted to DFT data and taking van der Waals corrections into account.

## 2. COMPUTATIONAL METHODOLOGY

**2.1. DFT Calculations.** All DFT calculations were performed using the Vienna Ab initio Simulation Package,[48−51] using the projector augmented wave method (PAW) with a plane-wave basis set.[52,53] Different exchange−correlation functionals were tested. In all cases, a cutoff energy of 600 eV was used with a 5 × 5 × 5 Γ-centered $k$-point mesh. Gaussian smearing was employed with $\sigma$ = 0.2 eV. Convergence thresholds for electronic and ionic SC loops were set to $10^{-6}$ and $10^{-5}$ eV, respectively. Ab initio molecular dynamics (AIMD) simulations to collect the initial data set for training the MLIP were run at 1000 K for 1 ps with a time step of 1 fs with the NPT ensemble and the Langevin thermostat for the 1 × 1 × 1 unit cell, containing 104 atoms.

The phonon band structure and phonon density of states were calculated using the finite displacement method,[54] as implemented in the Phonopy package[55] for the 1 × 1 × 1 unit cell.

**2.2. MLIP Construction.** Moment tensor potentials (MTPs) were constructed in two steps using the MLIP-3 code.[41,42,56−58] At the first step, the initial potential was built based on the initial data set from AIMD at 1000 K. At the second step, the initial potential was actively retrained during the heating simulation. Molecular dynamics simulations for active learning were performed using the LAMMPS[59,60] code. NPT simulations were performed for 1 ns with a time step of 1 fs with the Nose−Hoover thermostat[61,62] for the heating from 0 to 1000 K to cover all relevant configurations corresponding to different temperatures and 10 ns annealing simulations at 1000 K. The potential was retrained every time the grade of configurations exceeded the break threshold parameter, which was set to 11. The 20th level of MTP was used for training the potential.[58]

**2.3. Molecular Dynamics Simulations.** Molecular dynamics simulations were performed using the LAMMPS code in the NPT ensemble with the Nose−Hoover thermostat. A 3 × 3 × 3 supercell of $Li_2B_{12}H_{12}$ with 2808 atoms was used. Heating was performed from 0 to 1000 K for 1 ns with a time step of 0.5 fs. Diffusion simulations were carried out at temperatures from 200 to 700 K with an increase of 25 K for self-diffusion and 100 K for diffusion in a vacancy-rich material. Each simulation was performed for 1 ns (0.5 fs time step) with preliminary heating from 0 K to target temperature and equilibration for 0.2 ns.

Diffusion coefficients were calculated from the mean squared displacements (MSDs) of $Li^+$ cations

$$D = \frac{1}{6}\frac{\mathrm{d}}{\mathrm{d}t}\frac{1}{N}\sum_{j=1}^{N}\langle |r_j(t) - r_j(0)|^2 \rangle \quad (1)$$

where $N$ is the number of mobile atoms, $r_j(t)$ is the position vector of the $j$th atom after time $t$.

The ionic conductivity of the mobile cation (lithium) was calculated using the Nernst−Einstein formula


https://doi.org/10.1021/acsami.3c07242
ACS Appl. Mater. Interfaces 2023, 15, 42511−42519

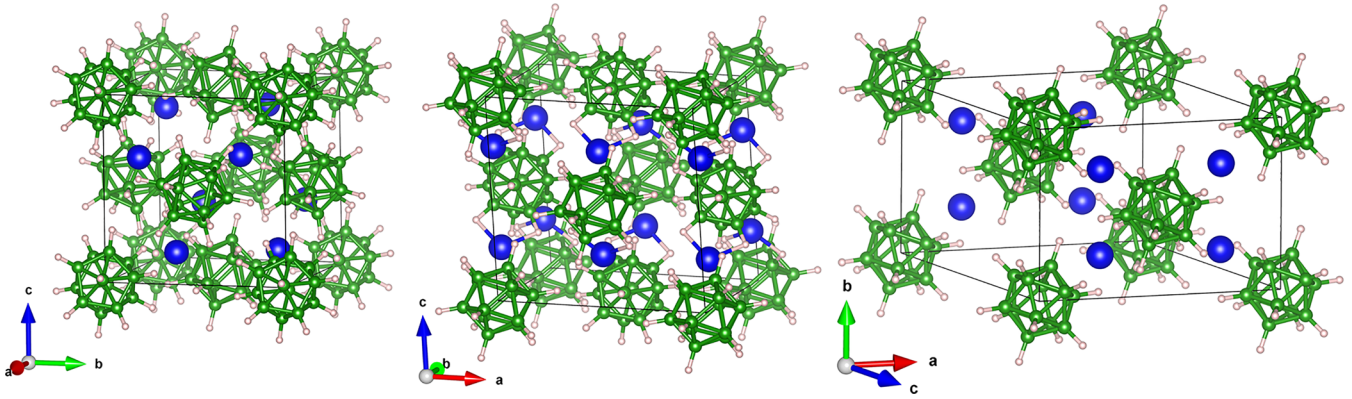


**Figure 1.** Crystal structures of $Li_2B_{12}H_{12}$: large (shown in blue), middle (green), and small (peach) spheres represent Li, B, and H atoms, respectively. (a) Cubic $Pa\bar{3}$ structure ($\alpha$-phase), (b) monoclinic $P2_1/n$ *structure, and (c) monoclinic C2/m structure.*

$$\sigma = \frac{nq^2D}{H_r k_B T} \tag{2}$$

where $n$ is the $Li^+$ ion density, $q$ is the charge of the $Li^+$ ion, $k_B$ is the Boltzmann constant, $T$ is the temperature, and $H_r$ is the Haven ratio (assumed to be 1).

Activation energy $E_a$ is the characteristic energy required for diffusion to occur. It was calculated using the Arrhenius formula

$$\sigma = \sigma_0 \exp\left(-\frac{E_a}{k_B T}\right) \tag{3}$$

## 3. RESULTS AND DISCUSSION

**3.1. Crystal Structure and the Effect of Exchange−Correlation Functionals.** The $Pa\bar{3}$ phase of $Li_2B_{12}H_{12}$ was confirmed in experiments using XRPD spectroscopy[31] and neutron vibrational spectroscopy.[63] DFT calculations with the PBE functional[64] incorrectly show $P2_1/c$ and $C2/m$ phases to be more stable,[38] earlier the importance of van der Waals interactions was demonstrated by Maniadaki and Łodziana;[39] however, previous DFT and AIMD calculations of $Li_2B_{12}H_{12}$[35,37,38] were performed only with the PBE exchange−correlation functional. In our study, we fully relaxed these three structures with different functionals. Optimized lattice parameters and relative energies are given in Table S1 in the Supporting Information. Crystal structures are shown in Figure 1. One can see that all functionals taking into account the van der Waals correction correctly predict the $Pa\bar{3}$ phase to be more stable and van der Waals interactions are essential. However, it is not clear which particular functional is best suited for closo-borane salts. As we are interested in dynamics and activation barriers, it is wise to use phonon frequencies as a criterion of accuracy of theory. Fortunately, neutron vibrational spectroscopy data have been collected at 4 K, and peak positions and intensities of the phonon spectrum can be compared with the calculated ones. Calculated phonon DOS of the $Pa\bar{3}$ phase (Figure S1 in the Supporting Information) with different functionals showed that Rev-vdW-DF2[65] describes peak positions and intensities in the closest agreement to the experiment. Notably, despite the wrong energetic description of the $Li_2B_{12}H_{12}$ structure, the PBE potential still describes the phonon spectrum of the $Pa\bar{3}$ phase reasonably well.

**3.2. Construction of Machine Learning Interatomic Potentials.** For $Li_2B_{12}H_{12}$, three different machine learning interatomic potentials were constructed based on PBE,[64] rev-vdW-DF2,[65] and PBE-D3[66] functionals. Rev-vdW-DF2 is the closest to the experiment in the description of phonon spectra; the PBE-based potential was constructed to compare it with the potentials including van der Waals interaction and evaluating its accuracy. PBE-D3 is a functional that is commonly used for energy and geometry prediction in systems with van der Waals interactions and is known[67] to yield good results at a reasonably low cost.

Statistics on the constructed MLIPs are provided in Table 1. More details can be found in Table S2 and Figures S2−S4 in the Supporting Information. For all constructed MLIPs, energy RMS errors are less than 5 meV/atom, and force RMS errors are about 0.05 eV/Å for the validation set.

**Table 1. Accuracy of Machine Learning Interatomic Potentials**

| | functional | | |
|---|---|---|---|
| | PBE | rev-vdW-DF2 | PBE-D3 |
| initial data set size | 400 | 630 | 633 |
| total data set size | 1222 | 1791 | 2409 |
| energy per atom range, eV/atom | −5.08/−4.90 | −4.77/−4.59 | −5.22/−5.03 |
| force range, eV/Å | −8/8 | −15/12 | −10/10 |
| stress range, kbar | −60/60 | −80/60 | −80/80 |
| energy per atom RMSE, eV/atom | 0.008 | 0.001 | 0.009 |
| force RMSE, eV/Å | 0.207 | 0.083 | 0.101 |
| stresses RMSE, kbar | 2.576 | 1.116 | 2.26 |

**3.3. Simulation of Diffusion and Phase Transitions.** *3.3.1. Temperature-Induced Phase Transition.* At the first stage of simulations, we performed the molecular dynamics of the heating process from 0 to 1000 K within PBE-based, PBE-D3, and rev-vdW-DF2-based interatomic potentials for $Li_2B_{12}H_{12}$. Figure 2a shows the lattice parameter as a function of temperature for all MLIPs. From the experiment, we know that there is a phase transition from $\alpha$-$Li_2B_{12}H_{12}$ ($Pa\bar{3}$ phase) into $\beta$-$Li_2B_{12}H_{12}$ (disordered phase) at 628 K; the lattice parameters are 9.58 and 10.01 Å at room temperature and 800 K, respectively. All potentials predict phase transition from the $\alpha$- to $\beta$-phase but differ in phase transition temperature and lattice parameters. PBE-based MLIP greatly underestimates the phase transition temperature (179 K) and overestimates the values of the lattice parameters by 2−4%. On the contrary, the


https://doi.org/10.1021/acsami.3c07242
ACS Appl. Mater. Interfaces 2023, 15, 42511−42519

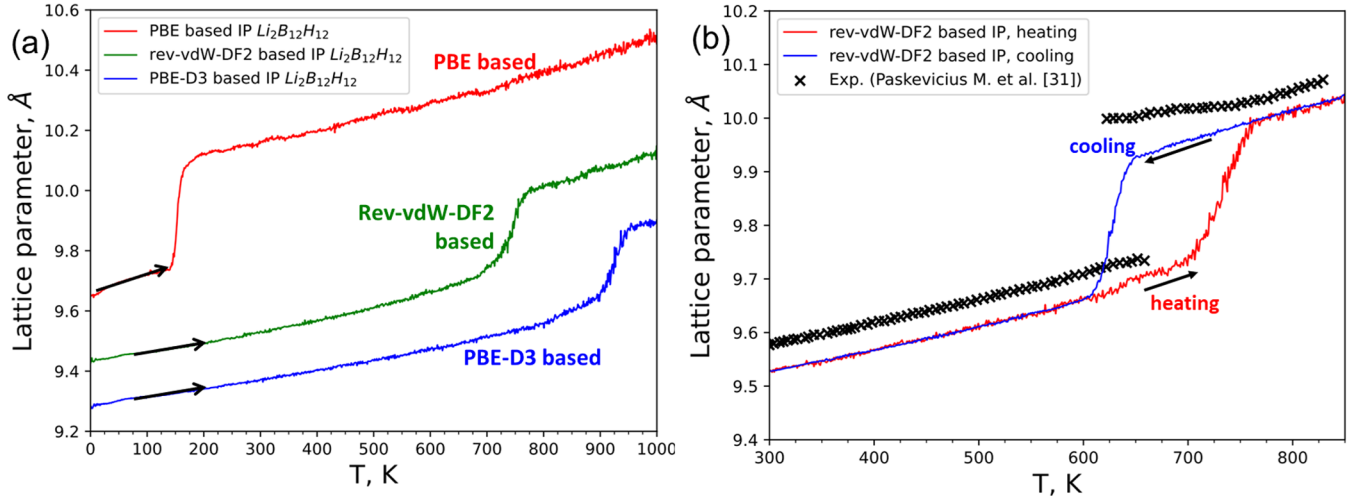


**Figure 2.** Lattice parameter of $Li_2B_{12}H_{12}$ as a function of temperature: (a) for PBE-based (red, top), rev-vdW-DF2-based (green, middle), and PBE-D3-based (blue, bottom) interatomic potentials during heating and (b) during heating (1 K/ps) and cooling (0.1 K/ps) simulations with the rev-vdW-DF2-based MLIP and experimental values.[31]

PBE-D3 potential overestimates the phase transition temperature (950 K) and underestimates the values of the lattice parameters by 2−5%. The rev-vdW-DF2-based MLIP is the closest one to the experiment (Figure 2b) with a phase transition temperature of 675 K. It underestimates the lattice parameter by less than 0.5% within the entire temperature range. Calculated lattice parameters are provided in Table 2.

**Table 2. Lattice Parameters of the $Li_2B_{12}H_{12}$ Unit Cell, Calculated Using Rev-vdW-DF2-Based MLIP at Different Temperatures**

| | lattice parameter, Å | |
|---|---|---|
| *T*, K | rev-vdW-DF2-MLIP | experiment[31] |
| 300 | 9.53 ± 0.03 | 9.58 |
| 600 | 9.66 ± 0.03 | 9.71 |
| 650 | 9.69 ± 0.03 | 9.73 |
| 800 | 10.01 ± 0.04 | 10.05 |

Heating and cooling simulations (Figure 2b) show a clear hysteresis in the lattice parameter temperature curve with half-height values at 725 K (heating) and 625 K (cooling) and an average value of 675 K. As the heating and cooling rates decrease, the hysteresis loop is expected to get narrower.

In the $\beta$-phase, there is a disordered arrangement of $Li^+$ ions (importantly, most of the time, they occupy tetrahedral voids) and an orientational disorder of $B_{12}H_{12}^{2-}$ anions. The symmetry of such a disordered structure is $Fm\bar{3}m$, which can be described as a $Li_2O$-like structure, where the role of anions is played not by oxygen ions but by dodecaboranes. $Li_2O$ is an ionic conductor,[68,69] and the larger cation−anion distance in $Li_2B_{12}H_{12}$ suggests that it will be an even better conductor.

One can see that the rev-vdW-DF2-based MLIP is the most accurate in terms of the phase transition and structural description, which is why we use it for further diffusion simulations.

*3.3.2. Self-Diffusion in $Li_2B_{12}H_{12}$.* At the second stage of calculations, we simulated the self-diffusion of $Li^+$ cation in the

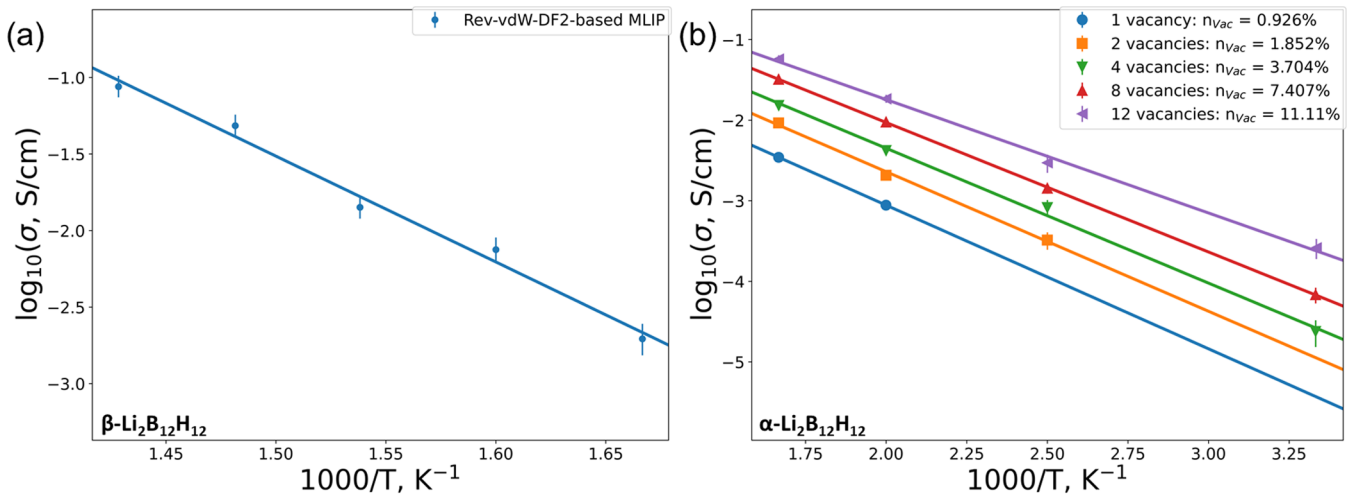


**Figure 3.** Ionic conductivity as a function of temperature calculated using the rev-vdW-DF2-based MLIP: (a) for the high-temperature $\beta$-$Li_2B_{12}H_{12}$ without vacancies and (b) for $\alpha$-$Li_2B_{12}H_{12}$ with different concentrations of vacancies; vertical bars denote statistical errors; at temperatures above 400 K and high vacancy concentrations, the errors are small.



https://doi.org/10.1021/acsami.3c07242
ACS Appl. Mater. Interfaces 2023, 15, 42511−42519

absence of vacancies in the temperature range between 200 and 700 K using the rev-vdW-DF2-based MLIP. Figure 3a shows the ionic conductivity versus $1/T$ for the high-temperature $\beta$-$Li_2B_{12}H_{12}$ phase. The simulations indicate that there is almost no self-diffusion in the low-temperature phase below 500 K, and self-diffusion starts simultaneously with the phase transition to the high-temperature $\beta$-phase. With the increase in temperature from 500 to 700 K, diffusion coefficients rise from $10^{-8}$ to $10^{-5}$ $cm^2/s$, and ionic conductivity varies from $10^{-4}$ to $10^{-1}$ S/cm, the activation barrier for ionic conductivity is 1.52 eV in the high temperature $\beta$-phase in the absent of vacancies and using rev-vdW-DF2 based MLIP. The fact that high ionic conductivity is only achieved in the $\beta$-$Li_2B_{12}H_{12}$ phase is consistent with previous studies.[26,27,31] Considerable discrepancies with experimental values in ref 23 of activation energy (0.34 eV) and ionic conductivity ($10^{-3}$ S/cm at room temperature) may be explained by the fact that MD simulations were performed for the single crystal with no vacancies, while the experiment is for a powder, where ball milling causes the formation of defect-rich microstructures that contribute to an increase in ion mobility, providing new pathways for $Li^+$ conduction.

Because the PBE-D3-based MLIP predicts phase transition to the high-temperature $\beta$-$Li_2B_{12}H_{12}$ phase only at temperatures higher than 900 K, there is no diffusion at temperatures below 900 K, as well as for the low-temperature phase within the rev-vdW-DF2-based MLIP results.

Diffusion coefficients and activation energy of diffusion of the high-temperature $\beta$-$Li_2B_{12}H_{12}$ phase calculated using PBE-based MLIP match the previous AIMD calculations:[35] Varley et al. obtained values of 136 meV, while in our MD simulations, we obtained it to be 147 meV. Diffusion coefficients at 700 K are about $10^{-4}$ $cm^2/s$ in both AIMD calculations[35] and our MD (Figure S5 in the Supporting Information). From this perspective, the constructed PBE-based MLIP reproduces DFT results with remarkable accuracy, and it is clear that the construction procedure of MLIP with active learning is reliable.

*3.3.3. Diffusion in $\alpha$-$Li_2B_{12}H_{12}$ with Vacancies.* Real materials always contain imperfections such as vacancies, which are essential for diffusion. To evaluate the dependence of ionic conductivity on vacancy concentration, we performed MD simulations with vacancy-rich supercells, which included 1, 2, 4, 8, and 12 vacancies (vacancy molar fractions were 0.93, 1.85, 3.70, 7.41, and 11.11%, respectively). Figure 3b shows the dependence of the ionic conductivity of supercells with vacancies on $1/T$. Activation energies are presented in Table 3.

**Table 3. Activation Energies of Diffusion in the $\alpha$-$Li_2B_{12}H_{12}$ Phase with Vacancies, Calculated Using Rev-vdW-DF2-Based MLIP**

| number of vacancies | vacancy concentration, mol % | activation energy, meV[a] |
|---|---|---|
| 1 | 0.926 | 353 |
| 2 | 1.852 | 343 |
| 4 | 3.704 | 332 |
| 8 | 7.407 | 320 |
| 12 | 11.11 | 279 |

[a]The experimental value is 340 meV.[23]

As can be seen from Figure 3, when a vacancy is introduced into the crystal, the ionic conductivity increases by several orders of magnitude. Compared with $\alpha$-$Li_2B_{12}H_{12}$ without vacancies, in which diffusion and ionic conductivity are absent, the introduction of a single vacancy results in the ionic conductivity in $\alpha$-$Li_2B_{12}H_{12}$ of up to $10^{-3}$ S/cm at 500 K. A subsequent increase in the vacancy concentration leads to a surge in diffusion, and an ionic conductivity of about $10^{-3}$ S/cm can be achieved already at 300 K. An increase in the concentration of vacancies occurs together with a decrease in the activation energy. Notably, the values of activation energies at realistic concentrations of vacancies (<3.7%) are 332−353 meV, which matches the experimental values of 340 meV obtained by Teprovich et al.[23] (Table 3). With a vacancy concentration of less than 2% and $T$ < 400 K, the ionic conductivities are small and because of large statistical errors are not shown in Figure 3.

*3.3.4. Rotational Motion of the $B_{12}H_{12}^{2-}$ Anion.* To obtain insights into the nature of the disordered $\beta$-$Li_2B_{12}H_{12}$ phase, we calculated the dependence of the $\theta(t)$ and $\varphi(t)$ angles (in spherical coordinates) of $r(t)$ (Figures 4 and S6) and angular autocorrelation functions $\xi(t) = \langle r(t)\cdot r(0)\rangle$ (Figure 5), where $r(t)$ is the radius vector from the center of mass of a given $B_{12}H_{12}$ cluster to one hydrogen of the cluster, and $\langle r(t)\cdot r(0)\rangle$ denotes an average scalar product over all trajectories. $B_{12}H_{12}^{2-}$ anions in structures with low vacancy concentration rotate with maximum deflection angles from ∼20° at 200 K to ∼45° at 700 K. Notably, within the rev-vdD-DF2-based MLIP calculation, there is no full rotation of the anions in the system without vacancies, in contrast to less reliable methods.[22,35] Full rotation of the anion is only observed at 700 K with a high vacancy concentration (7.4−11 mol %, Figure 4). A decrease in either temperature or vacancy concentration leads to the freezing of rotation, and only oscillations are observed (Figure S6 in the Supporting Information). The rotation of $B_{12}H_{12}^{2-}$ at a vacancy concentration of 7.4 mol % becomes uncorrelated in 0.4 ns. Rotation of $B_{12}H_{12}^{2-}$ at a vacancy concentration of 11.1 mol % becomes uncorrelated (Figure 5b) in just 20 ps. Thus, one can conclude that the high-temperature phase is statically disordered with a high activation energy of rotation and without dynamical disordering. Previous research[35−38] that used the PBE functional and AIMD, where dynamic disorder and full rotation were seen, are less reliable because of the underestimation of the anion−anion interaction and lack of van der Waals corrections, which are important in this system.

*3.3.5. Calculations of Phase Transitions and Ionic Conductivity in $LiCB_{11}H_{12}$.* We constructed a MLIP based on the rev-vdW-DF2 DFT functional and performed similar simulations for the closely related $LiCB_{11}H_{12}$ solid electrolyte using the same computational technique. A 1 × 1 × 1 unit cell with 100 atoms was used for the MLIP construction, while a 3 × 3 × 3 supercell with 2700 atoms was utilized for simulations. Figures S7 and S8 in the Supporting Information show the volume of a unit cell and ionic conductivity as functions of temperature. The phase transition temperature is 650 K, which is approximately 250 K higher than the experimental values. The ionic conductivity at room temperature is ∼$10^{-6}$−$10^{-5}$ S/cm and ∼$10^{-1}$−1 S/cm for the high-temperature phase, which matches the experimental value.[29] The activation energy of ionic conductivity at the low-temperature phase is 467 meV, which also agrees with the experimental value of 550 meV.[29]


https://doi.org/10.1021/acsami.3c07242
ACS Appl. Mater. Interfaces 2023, 15, 42511−42519

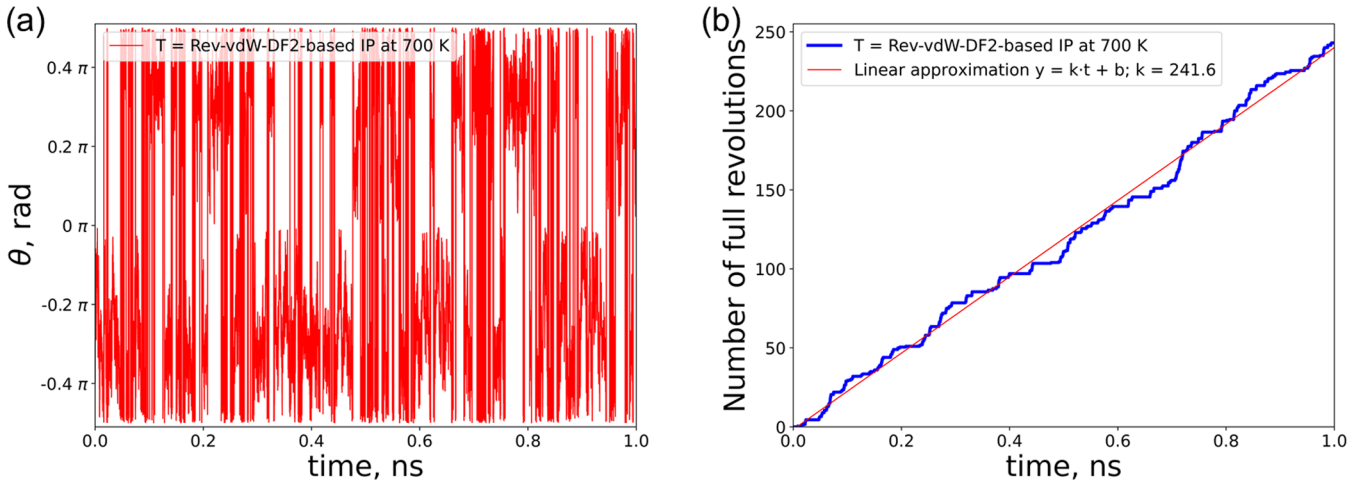


**Figure 4.** Angle of radius vector ($\theta$) from the $B_{12}H_{12}^{2-}$ center of mass to the adjusted boron atom as a function of time in the high-temperature $\beta$-phase of $Li_2B_{12}H_{12}$ at 700 K with 12 vacancies in the supercell ($n_{vac}$ = 11.11%) (a), and a total number of full rotations (b).

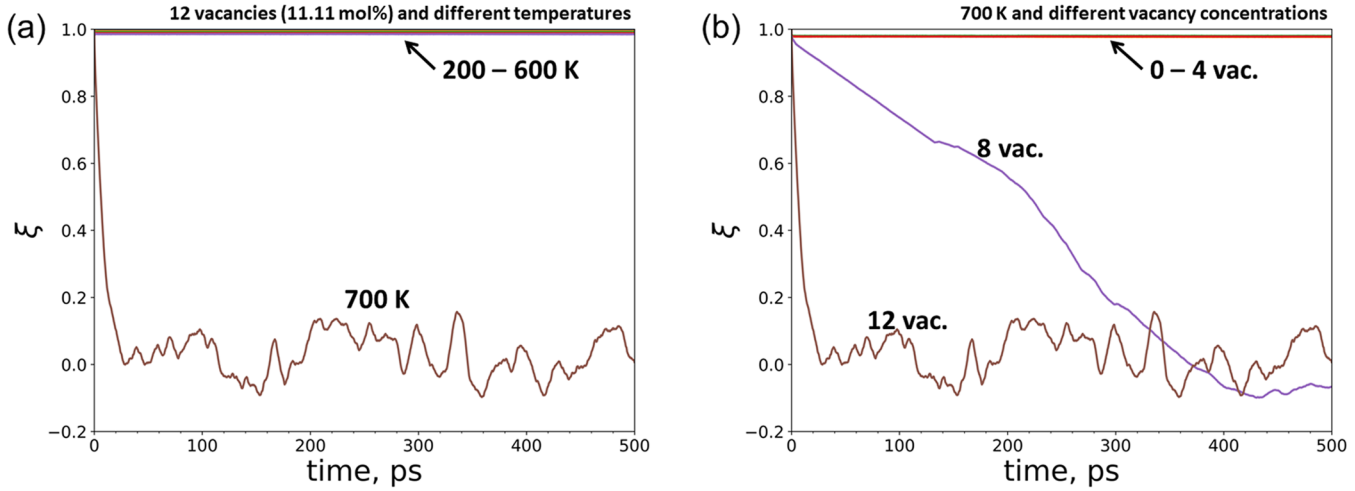


**Figure 5.** Angular autocorrelation function $\xi(t)$ of the $B_{12}H_{12}^{2-}$ anion as a function of time from the rev-vdW-DF2-based MLIP simulation with respect to (a) temperature and (b) vacancy concentration.

## 4. CONCLUSIONS

Three different machine learning interatomic potentials (MLIPs), based on PBE, rev-vdW-DF2, and PBE-D3 data sets, were built for $Li_2B_{12}H_{12}$. It has been shown that the rev-vdW-DF2 functional is the best one among all considered functionals to predict the phonon DOS spectrum, and, as a result, the MLIP based on it predicts phase transition temperature and lattice parameters in the temperature range from 0 to 1000 K with high accuracy.

Diffusion simulations have shown that $Li_2B_{12}H_{12}$ without vacancies has almost no self-diffusion of $Li^+$ cations in the low-temperature $\alpha$-$Li_2B_{12}H_{12}$ phase, while in the high-temperature $\beta$-$Li_2B_{12}H_{12}$ phase, a superionic state is achieved with the ionic conductivity of up to $10^{-1}$ S/cm at 700 K. In contrast to the perfect $Li_2B_{12}H_{12}$, a high diffusion rate is obtained both in $\alpha$- and $\beta$-phases of $Li_2B_{12}H_{12}$ with vacancies and is about $10^{-4}$–$10^{-3}$ S/cm at room temperature. The calculated activation energy for ionic conductivity is 343 meV at a vacancy concentration of 2 mol %.

The reorientation motion of the $B_{12}H_{12}^{2-}$ anion is responsible for the superionic behavior and static orientation disorder in the high-temperature $\beta$-phase and high ionic conductivity in the $\alpha$-phase with vacancies, although in most cases, there is no full rotation of the anion. Instead, the observed rotation is up to 15−45°. It has been shown that in special cases of high temperature and high vacancy concentration, reorientation motion becomes full rotation with an approximate number of revolutions from 200 to 300 per 1 ns.

The MLIP constructed based on rev-vdW-DF2 data for $LiCB_{11}H_{12}$ also describes phase transition and ionic conductivity of room and high-temperature phases matching the experiment; the activation energy of ionic conductivity of the low-temperature phase is 467 meV; the ionic conductivity at room temperature is $10^{-6}$–$10^{-5}$ S/cm and up to 1 S/cm in the high-temperature phase.

$Li_2B_{12}H_{12}$ and $LiCB_{11}H_{12}$ are promising solid electrolytes for all-solid-state lithium batteries.

## ■ ASSOCIATED CONTENT

### Supporting Information

The Supporting Information is available free of charge at https://pubs.acs.org/doi/10.1021/acsami.3c07242.



https://doi.org/10.1021/acsami.3c07242
ACS Appl. Mater. Interfaces 2023, 15, 42511−42519

Phonon dispersion DOS calculated with the use of different DFT functionals (Figure S1); energy (a), force (b), and stress (c) errors of the validation data set and their distribution calculated with PBE-based IP. AAE and RMSE denote the average absolute error and RMS error, respectively, between DFT and MLIP data of the validation set (Figure S2); energy (a), force (b), and stress (c) errors of the validation data set and their distribution calculated with PBE-D3-based IP. AAE and RMSE denote the average absolute error and RMS error, respectively, between DFT and MLIP data of the validation set (Figure S3); energy (a), force (b), and stress (c) errors of the validation data set and their distribution calculated with rev-vdW-DF2-based IP. AAE and RMSE denote the average absolute error and RMS error, respectively, between DFT and MLIP data of the validation set (Figure S4); diffusion coefficients as a function of temperature, calculated using PBE-based MLIP for the high-temperature $\beta$-$Li_2B_{12}H_{12}$ phase (Figure S5); time dependence of $\theta$ and $\varphi$ angles in spherical coordinates of the radius vector from the $B_{12}H_{12}^{2-}$ center of mass to a given hydrogen atom at different temperatures in $Li_2B_{12}H_{12}$ without vacancies (Figure S6); $LiCB_{11}H_{12}$ unit cell volume as a function of temperature, calculated with rev-vdW-DF2-based MLIP (Figure S7); ion conductivity as a function of temperature for $LiCB_{11}H_{12}$ with vacancies, calculated with rev-vdW-DF2-based MLIP. LT-phase and HT-phase denote low- and high-temperature phases, respectively (Figure S8); $Pa\bar{3}$ phase: lattice parameters and peaks of phonon DOS (Table S1a), $P21/c$ phase: lattice parameters and total energy relative to the $Pa\bar{3}$ phase (Table S1b), and $C2/m$ phase: lattice parameters and total energy relative to the $Pa\bar{3}$ phase (Table S1c); and errors in the training sets of the MLIPs constructed with different DFT functionals (Table S2) (PDF)

## AUTHOR INFORMATION


### Corresponding Author

**Alexey P. Maltsev** − *Skolkovo Institute of Science and Technology, Moscow 121205, Russia;* orcid.org/0000-0003-4352-7673; Email: alexey.maltsev@skoltech.ru

### Authors

**Ilya V. Chepkasov** − *Skolkovo Institute of Science and Technology, Moscow 121205, Russia;* orcid.org/0000-0001-8376-2999

**Artem R. Oganov** − *Skolkovo Institute of Science and Technology, Moscow 121205, Russia;* orcid.org/0000-0001-7082-9728

Complete contact information is available at: https://pubs.acs.org/10.1021/acsami.3c07242


### Notes

The authors declare no competing financial interest.

## ACKNOWLEDGMENTS

This work was supported financially by the Russian Science Foundation. A.R.O. thanks grant no. 19-72-30043 for the DFT calculations. A.P.M and I.V.C. thank grant no. 22-73-00219 for the molecular dynamics simulations of phase transitions and ionic conductivity.

## REFERENCES


(1) Xu, J.; Dou, Y.; Wei, Z.; Ma, J.; Deng, Y.; Li, Y.; Liu, H.; Dou, S. Recent Progress in Graphite Intercalation Compounds for Rechargeable Metal (Li, Na, K, Al)-ion Batteries. *Adv. Sci.* **2017**, *4*, No. 1700146.

(2) Janek, J.; Zeier, W. G. A Solid Future for Battery Development. *Nat. Energy* **2016**, *1*, No. 16141.

(3) Tarascon, J.-M.; Armand, M. Issues and Challenges Facing Rechargeable Lithium Batteries. *Nature* **2001**, *414*, 359−367.

(4) Xu, W.; Wang, J.; Ding, F.; Chen, X.; Nasybulin, E.; Zhang, Y.; Zhang, J.-G. Lithium Metal Anodes for Rechargeable Batteries. *Energy Environ. Sci.* **2014**, *7*, 513−537.

(5) Armand, M.; Tarascon, J.-M. Building Better Batteries. *Nature* **2008**, *451*, 652−657.

(6) Sakuda, A.; Kitaura, H.; Hayashi, A.; Tadanaga, K.; Tatsumisago, M. All-solid-state Lithium Secondary Batteries with Oxide-Coated $LiCoO_2$ Electrode and $Li_2S$−$P_2S_5$ Electrolyte. *J. Power Sources* **2009**, *189*, 527−530.

(7) Sakuda, A.; Hayashi, A.; Tatsumisago, M. Interfacial Observation between $LiCoO_2$ Electrode and $Li_2S$- $P_2S_5$ Solid Electrolytes of All-Solid-State Lithium Secondary Batteries Using Transmission Electron Microscopy. *Chem. Mater.* **2010**, *22*, 949−956.

(8) Nagao, M.; Hayashi, A.; Tatsumisago, M.; Kanetsuku, T.; Tsuda, T.; Kuwabata, S. In Situ SEM Study of a Lithium Deposition and Dissolution Mechanism in a Bulk-type Solid-state Cell with a $Li_2S$−$P_2S_5$ Solid Electrolyte. *Phys. Chem. Chem. Phys.* **2013**, *15*, 18600−18606.

(9) Liu, Z.; Fu, W.; Payzant, E. A.; Yu, X.; Wu, Z.; Dudney, N. J.; Kiggans, J.; Hong, K.; Rondinone, A. J.; Liang, C. Anomalous High Ionic Conductivity of Nanoporous $\beta$-$Li_3PS_4$. *J. Am. Chem. Soc.* **2013**, *135*, 975−978.

(10) Lepley, N. D.; Holzwarth, N. Modeling Interfaces between Solids: Application to Li Battery Materials. *Phys. Rev. B* **2015**, *92*, No. 214201.

(11) Kamphaus, E. P.; Balbuena, P. B. Polysulfide Reduction and $Li_2S$ Phase Formation in the Presence of Lithium Metal and Solid Electrolyte Interphase Layer. *J. Power Sources* **2021**, *485*, No. 229289.

(12) Erika, N.; Arthur, T. S.; Bonnick, P.; Suto, K.; Muldoon, J. The Discharge Mechanism for Solid-state Lithium-Sulfur Batteries. *MRS Adv.* **2019**, *4*, 2627−2634.

(13) Song, Y.-X.; Shi, Y.; Wan, J.; Lang, S.-Y.; Hu, X.-C.; Yan, H.-J.; Liu, B.; Guo, Y.-G.; Wen, R.; Wan, L.-J. Direct Tracking of the Polysulfide Shuttling and Interfacial Evolution in All-solid-state Lithium−sulfur Batteries: a Degradation Mechanism Study. *Energy Environ. Sci.* **2019**, *12*, 2496−2506.

(14) Shutthanandan, V.; Nandasiri, M.; Zheng, J.; Engelhard, M. H.; Xu, W.; Thevuthasan, S.; Murugesan, V. Applications of XPS in the Characterization of Battery Materials. *J. Electron Spectrosc. Relat. Phenom.* **2019**, *231*, 2−10.

(15) Wenzel, S.; Weber, D. A.; Leichtweiss, T.; Busche, M. R.; Sann, J.; Janek, J. Interphase Formation and Degradation of Charge Transfer Kinetics between a Lithium Metal Anode and Highly Crystalline $Li_7P_3S_{11}$ Solid Electrolyte. *Solid State Ionics* **2016**, *286*, 24−33.

(16) Rangasamy, E.; Liu, Z.; Gobet, M.; Pilar, K.; Sahu, G.; Zhou, W.; Wu, H.; Greenbaum, S.; Liang, C. An Iodide-based $Li_7P_2S_8I$ Superionic Conductor. *J. Am. Chem. Soc.* **2015**, *137*, 1384−1387.

(17) Wenzel, S.; Sedlmaier, S. J.; Dietrich, C.; Zeier, W. G.; Janek, J. Interfacial Reactivity and Interphase Growth of Argyrodite Solid Electrolytes at Lithium Metal Electrodes. *Solid State Ionics* **2018**, *318*, 102−112.

(18) Wenzel, S.; Randau, S.; Leichtweiß, T.; Weber, D. A.; Sann, J.; Zeier, W. G.; Janek, J. Direct Observation of the Interfacial Instability of the Fast Ionic Conductor $Li_{10}GeP_2S_{12}$ at the Lithium Metal Anode. *Chem. Mater.* **2016**, *28*, 2400−2407.

(19) Kato, Y.; Saito, R.; Sakano, M.; Mitsui, A.; Hirayama, M.; Kanno, R. Synthesis, Structure and Lithium Ionic Conductivity of Solid Solutions of $Li_{10}(Ge_{1-x}M_x)P_2S_{12}$ (M= Si, Sn). *J. Power Sources* **2014**, *271*, 60−64.

(20) Kwon, O.; Hirayama, M.; Suzuki, K.; Kato, Y.; Saito, T.; Yonemura, M.; Kamiyama, T.; Kanno, R. Synthesis, Structure, and Conduction Mechanism of the Lithium Superionic Conductor $Li_{10+\delta}Ge_{1+\delta}P_{2-\delta}S_{12}$. *J. Mater. Chem. A* **2015**, *3*, 438−446.
(21) He, L.; Li, H.-W.; Nakajima, H.; Tumanov, N.; Filinchuk, Y.; Hwang, S.-J.; Sharma, M.; Hagemann, H.; Akiba, E. Synthesis of a Bimetallic Dodecaborate $LiNaB_{12}H_{12}$ with Outstanding Superionic Conductivity. *Chem. Mater.* **2015**, *27*, 5483−5486.
(22) Sau, K.; Ikeshoji, T.; Kim, S.; Takagi, S.; Orimo, S.-i. Comparative Molecular Dynamics Study of the Roles of Anion−cation and Cation−cation Correlation in Cation Diffusion in $Li_2B_{12}H_{12}$ and $LiCB_{11}H_{12}$. *Chem. Mater.* **2021**, *33*, 2357−2369.
(23) Teprovich, J. A.; Colón-Mercado, H.; Washington, A. L., II; Ward, P. A.; Greenway, S.; Missimer, D. M.; Hartman, H.; Velten, J.; Christian, J. H.; Zidan, R. Bi-functional $Li_2B_{12}H_{12}$ for Energy Storage and Conversion Applications: Solid-state Electrolyte and Luminescent Down-conversion Dye. *J. Mater. Chem. A* **2015**, *3*, 22853−22859.
(24) Unemoto, A.; Yoshida, K.; Ikeshoji, T.; Orimo, S.-i. Bulk-type All-solid-state Lithium Batteries Using Complex Hydrides Containing Cluster-anions. *Mater. Trans., JIM* **2016**, *57*, 1639−1644.
(25) Unemoto, A.; Ikeshoji, T.; Yasaku, S.; Matsuo, M.; Stavila, V.; Udovic, T. J.; Orimo, S.-i. Stable Interface Formation between $TiS_2$ and $LiBH_4$ in Bulk-type All-solid-state Lithium Batteries. *Chem. Mater.* **2015**, *27*, 5407−5416.
(26) Udovic, T. J.; Matsuo, M.; Unemoto, A.; Verdal, N.; Stavila, V.; Skripov, A. V.; Rush, J. J.; Takamura, H.; Orimo, S.-i. Sodium Superionic Conduction in $Na_2B_{12}H_{12}$. *Chem. Commun.* **2014**, *50*, 3750−3752.
(27) Udovic, T. J.; Matsuo, M.; Tang, W. S.; Wu, H.; Stavila, V.; Soloninin, A. V.; Skoryunov, R. V.; Babanova, O. A.; Skripov, A. V.; Rush, J. J.; et al. Exceptional Superionic Conductivity in Disordered Sodium Decahydro-closo-decaborate. *Adv. Mater.* **2014**, *26*, 7622−7626.
(28) Wu, H.; Tang, W. S.; Zhou, W.; Stavila, V.; Rush, J. J.; Udovic, T. J. The Structure of Monoclinic $Na_2B_{10}H_{10}$: A Combined Diffraction, Spectroscopy, and Theoretical Approach. *CrystEngComm* **2015**, *17*, 3533−3540.
(29) Tang, W. S.; Unemoto, A.; Zhou, W.; Stavila, V.; Matsuo, M.; Wu, H.; Orimo, S.-i.; Udovic, T. J. Unparalleled Lithium and Sodium Superionic Conduction in Solid Electrolytes with Large Monovalent Cage-like Anions. *Energy Environ. Sci.* **2015**, *8*, 3637−3645.
(30) Tang, W. S.; Matsuo, M.; Wu, H.; Stavila, V.; Zhou, W.; Talin, A. A.; Soloninin, A. V.; Skoryunov, R. V.; Babanova, O. A.; Skripov, A. V.; et al. Liquid-like Ionic Conduction in Solid Lithium and Sodium Monocarba-closo-decaborates Near or at Room Temperature. *Adv. Energy Mater.* **2016**, *6*, No. 1502237.
(31) Paskevicius, M.; Pitt, M. P.; Brown, D. H.; Sheppard, D. A.; Chumphongphan, S.; Buckley, C. E. First-order Phase Transition in the $Li_2B_{12}H_{12}$ System. *Phys. Chem. Chem. Phys.* **2013**, *15*, 15825−15828.
(32) Tang, W. S.; Dimitrievska, M.; Stavila, V.; Zhou, W.; Wu, H.; Talin, A. A.; Udovic, T. J. Order−disorder Transitions and Superionic Conductivity in the Sodium Nido-undeca (Carba) Borates. *Chem. Mater.* **2017**, *29*, 10496−10509.
(33) Ellis, B. L.; Nazar, L. F. Sodium and Sodium-ion Energy Storage Batteries. *Curr. Opin. Solid State Mater. Sci.* **2012**, *16*, 168−177.
(34) Hueso, K. B.; Armand, M.; Rojo, T. High Temperature Sodium Batteries: Status, Challenges and Future Trends. *Energy Environ. Sci.* **2013**, *6*, 734−749.
(35) Varley, J. B.; Kweon, K.; Mehta, P.; Shea, P.; Heo, T. W.; Udovic, T. J.; Stavila, V.; Wood, B. C. Understanding Ionic Conductivity Trends in Polyborane Solid Electrolytes from Ab Initio Molecular Dynamics. *ACS Energy Lett.* **2017**, *2*, 250−255.
(36) Sau, K.; Ikeshoji, T.; Kim, S.; Takagi, S.; Akagi, K.; Orimo, S.-i. Reorientational Motion and $Li^+$-ion Transport in $Li_2B_{12}H_{12}$ System: Molecular Dynamics Study. *Phys. Rev. Mater.* **2019**, *3*, No. 075402.
(37) Akrouchi, A.; Benzidi, H.; Al-Shami, A.; El kenz, A.; Benyoussef, A.; El Kharbachi, A.; Mounkachi, O. First-principles Study of Closo-dodecaborates $M_2B_{12}H_{12}$ (M= Li, Na, K) as Solid-state Electrolyte Materials. *Phys. Chem. Chem. Phys.* **2021**, *23*, 27014−27023.
(38) Li, S.; Ju, X.; Wan, C. First-principles Calculations of Structural, Elastic and Electronic Properties of $Li_2B_{12}H_{12}$. *J. Alloys Compd.* **2014**, *593*, 169−175.
(39) Maniadaki, A. E.; Łodziana, Z. Theoretical Description of Alkali Metal Closo-boranes − Towards the Crystal Structure of $MgB_{12}H_{12}$. *Phys. Chem. Chem. Phys.* **2018**, *20*, 30140−30149.
(40) Gubaev, K.; Podryabinkin, E. V.; Hart, G. L.; Shapeev, A. V. Accelerating High-throughput Searches for New Alloys with Active Learning of Interatomic Potentials. *Comput. Mater. Sci.* **2019**, *156*, 148−156.
(41) Podryabinkin, E. V.; Tikhonov, E. V.; Shapeev, A. V.; Oganov, A. R. Accelerating Crystal Structure Prediction by Machine-learning Interatomic Potentials with Active Learning. *Phys. Rev. B* **2019**, *99*, No. 064114.
(42) Körmann, F.; Kostiuchenko, T.; Shapeev, A.; Neugebauer, J. B2 Ordering in Body-centered-cubic AlNbTiV Refractory High-entropy Alloys. *Phys. Rev. Mater.* **2021**, *5*, No. 053803.
(43) Shapeev, A. V.; Podryabinkin, E. V.; Gubaev, K.; Tasnádi, F.; Abrikosov, I. A. Elinvar Effect in $\beta$-Ti Simulated by On-the-fly Trained Moment Tensor Potential. *New J. Phys.* **2020**, *22*, No. 113005.
(44) Novoselov, I.; Yanilkin, A.; Shapeev, A.; Podryabinkin, E. Moment Tensor Potentials as a Promising Tool to Study Diffusion Processes. *Comput. Mater. Sci.* **2019**, *164*, 46−56.
(45) Novikov, I. S.; Suleimanov, Y. V.; Shapeev, A. V. Automated Calculation of Thermal Rate Coefficients Using Ring Polymer Molecular Dynamics and Machine-learning Interatomic Potentials with Active Learning. *Phys. Chem. Chem. Phys.* **2018**, *20*, 29503−29512.
(46) Rosenbrock, C. W.; Gubaev, K.; Shapeev, A. V.; Pártay, L. B.; Bernstein, N.; Csányi, G.; Hart, G. L. Machine-learned Interatomic Potentials for Alloys and Alloy Phase Diagrams. *npj Comput. Mater.* **2021**, *7*, 24.
(47) Maltsev, A. P.; Chepkasov, I. V.; Kvashnin, A. G.; Oganov, A. R. Ionic Conductivity of Lithium Phosphides. *Crystals* **2023**, *13*, 756.
(48) Kresse, G.; Furthmüller, J. Efficient Iterative Schemes for Ab Initio Total-energy Calculations Using a Plane-wave Basis Set. *Phys. Rev. B* **1996**, *54*, 11169.
(49) Kresse, G.; Furthmüller, J. Efficiency of Ab Initio Total Energy Calculations for Metals and Semiconductors Using a Plane-wave Basis Set. *Comput. Mater. Sci.* **1996**, *6*, 15−50.
(50) Kresse, G.; Hafner, J. Ab Initio Molecular Dynamics for Liquid Metals. *Phys. Rev. B* **1993**, *47*, 558.
(51) Hafner, J. Materials Simulations Using VASP — a Quantum Perspective to Materials Science. *Comput. Phys. Commun.* **2007**, *177*, 6−13.
(52) Blöchl, P. E. Projector Augmented-wave Method. *Phys. Rev. B* **1994**, *50*, 17953.
(53) Kresse, G.; Joubert, D. From Ultrasoft Pseudopotentials to the Projector Augmented Wave Method. *Phys. Rev. B* **1999**, *59*, 1758.
(54) Parlinski, K.; Li, Z.; Kawazoe, Y. First-principles Determination of the Soft Mode in Cubic $ZrO_2$. *Phys. Rev. Lett.* **1997**, *78*, 4063.
(55) Togo, A.; Tanaka, I. First Principles Phonon Calculations in Materials Science. *Scr. Mater.* **2015**, *108*, 1−5.
(56) Novikov, I. S.; Gubaev, K.; Podryabinkin, E. V.; Shapeev, A. V. The MLIP Package: Moment Tensor Potentials with MPI and Active Learning. *Mach. Learn.: Sci. Technol.* **2020**, *2*, No. 025002.
(57) Shapeev, A. V. Moment Tensor Potentials: A Class of Systematically Improvable Interatomic Potentials. *Multiscale Model. Simul.* **2016**, *14*, 1153−1173.
(58) Podryabinkin, E. V.; Shapeev, A. V. Active Learning of Linearly Parametrized Interatomic Potentials. *Comput. Mater. Sci.* **2017**, *140*, 171−180.
(59) Plimpton, S. Fast Parallel Algorithms for Short-range Molecular Dynamics. *J. Comput. Phys.* **1995**, *117*, 1−19.

(60) Thompson, A. P.; Aktulga, H. M.; Berger, R.; Bolintineanu, D. S.; Brown, W. M.; Crozier, P. S.; in't Veld, P. J.; Kohlmeyer, A.; Moore, S. G.; Nguyen, T. D.; Shan, R.; Stevens, M. J.; Tranchida, J.; Trott, C.; Plimpton, S. J. LAMMPS − a Flexible Simulation Tool for Particle-based Materials Modeling at the Atomic, Meso, and Continuum Scales. *Comput. Phys. Commun.* **2022**, *271*, No. 108171.
(61) Hoover, W. G. Constant-pressure Equations of Motion. *Phys. Rev. A* **1986**, *34*, 2499−2500.
(62) Evans, D. J.; Holian, B. L. The Nose−Hoover Thermostat. *J. Chem. Phys.* **1985**, *83*, 4069−4074.
(63) Her, J.-H.; Yousufuddin, M.; Zhou, W.; Jalisatgi, S. S.; Kulleck, J. G.; Zan, J. A.; Hwang, S.-J.; Bowman, R. C., Jr.; Udovic, T. J. Crystal Structure of $Li_2B_{12}H_{12}$: a Possible Intermediate Species in the Decomposition of $LiBH_4$. *Inorg. Chem.* **2008**, *47*, 9757−9759.
(64) Perdew, J. P.; Burke, K.; Ernzerhof, M. Generalized Gradient Approximation Made Simple. *Phys. Rev. Lett.* **1996**, *77*, 3865−3868.
(65) Hamada, I. Van der Waals Density Functional Made Accurate. *Phys. Rev. B* **2014**, *89*, No. 121103.
(66) Grimme, S. Semiempirical GGA-type Density Functional Constructed With a Long-range Dispersion Correction. *J. Comput. Chem.* **2006**, *27*, 1787−1799.
(67) Momenzadeh Abardeh, Z.; Salimi, A.; Oganov, A. R. Crystal Structure Prediction of N-halide Phthalimide Compounds: Halogen Bonding Synthons as a Touchstone. *CrystEngComm* **2022**, *24*, 6066−6075.
(68) Minami, T.; Tatsumisago, M.; Wakihara, M.; Iwakura, C.; Kohjiya, S.; Tanaka, I. *Solid State Ionics for Batteries*; Springer, 2005.
(69) Islam, M. M.; Bredow, T. Density Functional Theory Study for the Stability and Ionic Conductivity of $Li_2O$ Surfaces. *J. Phys. Chem. C* **2009**, *113*, 672−676.




https://doi.org/10.1021/acsami.3c07242
*ACS Appl. Mater. Interfaces* 2023, 15, 42511−42519